Cell-to-Cell and Cycle-to-Cycle Retention Statistics in Phase-Change Memory Arrays

Maurizio Rizzi, Nicola Ciocchini, *Student Member, IEEE*, Anna Montefiori, Massimo Ferro, Paolo Fantini, Andrea L. Lacaita, *Fellow, IEEE*, and Daniele Ielmini, *Senior Member, IEEE*

I. Introduction

PHASE-CHANGE memory (PCM) is one of the strongest candidates for future generation nonvolatile memory (NVM) [1] with high speed [2], [3], small cell size, and a scalable power consumption [4]. Phase switching in $Ge_2Sb_2Te_5$ (GST) based cells, from amorphous (reset) to crystalline (set) and vice versa, can be rapid (<100 ns) in the high temperature (Joule heating) regime [5], [6]. On the other hand, the spontaneous transition of the metastable amorphous phase to the crystalline state, which limits the data retention, requires long times, (e.g., >10 years <85 °C) in the low temperature (bake) regime [7]. This allows for fast, rewritable memory, and NVM operation. To develop the next generation PCM technologies, it is crucial to gain a better understanding of the sources of variability, both at cell-to-cell and cycle-to-cycle levels, to optimize read/program algorithms to achieve the best performances [8]. To this purpose, this paper presents a thorough statistical characterization and Monte Carlo (MC) modeling of cell-to-cell and cycle-to-cycle statistics of data retention.

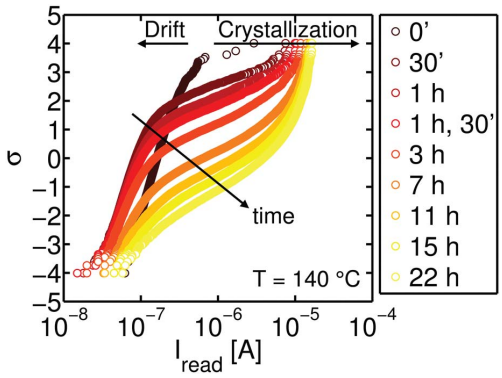

Fig. 1. Cumulative distributions of I_{read} as a function of the bake time. Cells, initially in the reset state, are annealed at 140 °C for increasingly longer times ranging from 30 min to 22 h. The reset distribution shows a narrow log-normal shape. Then, after the first bake step, slow cells show drift while fast cells show crystallization. By increasing the bake time, the final distribution increases its median value with a progressive crystallization.

Preliminary results of this paper were previously reported in [9] and [10]. In this paper, the MC model is extended to quantitatively predict the variability of crystallization rate at the array level, as a function of time and temperature. The analysis is further supported by an analytical theory based on the binomial statistics.

II. Experimental Technique

Fig. 1 shows the distributions of I_{read} during a bake experiment at $T = 140$ °C for increasing time. The initial low-conductive reset state moves toward the final state, eventually approaching the set state for increasing bake time.

This paper presents 16-kb array partitions with direct memory access readout mode, allowing to collect the read current for any cell within the array. The sample allows for a sufficient statistical accuracy in reasonable time for the characterization and data analysis [9].

In retention experiment, the array partition was first programmed at the reset state with a single box-like pulse with fast quenching time ($t_{quench} = 10$ ns), then the readout current distribution was measured at the voltage bias V_{read}. To speed up crystallization, cells were annealed for a time t

Manuscript received December 5, 2014; revised February 14, 2015 and April 7, 2015; accepted May 13, 2015. Date of publication June 2, 2015; date of current version June 17, 2015. The review of this paper was arranged by Editor U. E. Avci.

M. Rizzi, N. Ciocchini, and D. Ielmini are with the Dipartimento di Elettronica, Informazione e Bioingegneria, Italian Universities Nanoelectronics Team, Politecnico di Milano, Milan 20133, Italy (e-mail: maurizio1.rizzi@polimi.it; nicola.ciocchini@polimi.it; daniele.ielmini@polimi.it).

A. Montefiori was with the Dipartimento di Scienza dei Materiali, Università degli Studi di Milano–Bicocca, Milan 20126, Italy. She is now with Cobra Automotive Technologies, Varese 21100, Italy (e-mail: a.montefiori@campus.unimib.it).

M. Ferro and P. Fantini are with Micron Technology, Inc., Agrate Brianza 20864, Italy (e-mail: mferro@micron.com; pfantini@micron.com).

A. L. Lacaita is with the Dipartimento di Elettronica, Informazione e Bioingegneria, Italian Universities Nanoelectronics Team, Politecnico di Milano, Milan 20133, Italy, and also with the Istituto di Fotonica e Nanotecnologie, Consiglio Nazionale delle Ricerche, Milan 20133, Italy (e-mail: andrea.lacaita@polimi.it).

Color versions of one or more of the figures in this paper are available online.

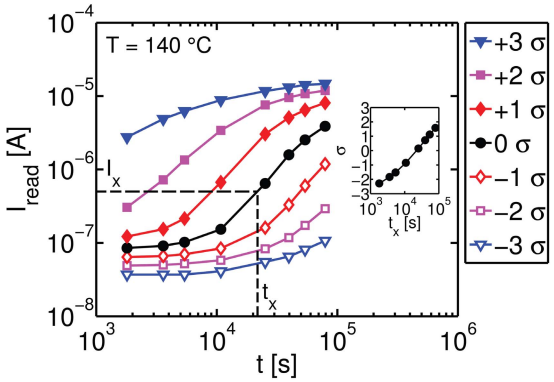

Fig. 2. I_{read} as a function of the bake time t taken from the distributions of Fig. 1 for equivalent cells in the range $-3 < \sigma < 3$. The different behaviors result in the spread of the crystallization time t_x, defined at the crossing of I_x. Inset: log-normal shape of the t_x cell-to-cell distribution.

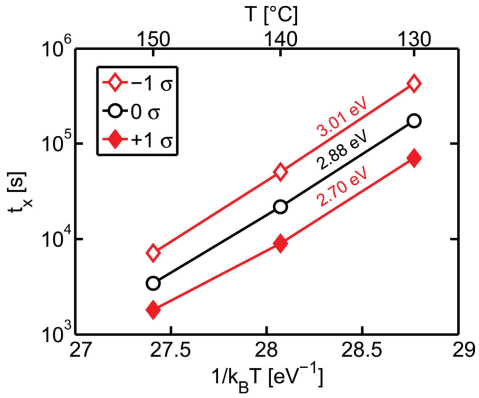

Fig. 3. Crystallization times t_x as a function of $1/k_BT$. Straight lines: Arrhenius dependence of crystallization. The slope E_x increases with sigma, causing the cell-to-cell spread of t_x.

at a temperature T in the range from 130 °C to 150 °C. This temperature range is much higher than the typical PCM operating temperature, which is <85 °C. Readout was repeated after every bake operation step, thus providing the distribution of read current I_{read} for a total bake time ranging from 30 min to 22 h. Read and program operations were both carried out at ambient temperature.

At the end of every bake series, all cells in the considered population were programmed in the set state, regardless of the postbake cell state, by means of a trapezoidal electrical pulse that first melts the chalcogenide and then slowly quenches it ($t_{\text{quench}} = 10\ \mu$s). In this way, every reset operation started from the same set state.

III. Cell-to-Cell Variability

The I_{read} distribution for cells programmed in the reset state is shown in Fig. 1 and displays a log-normal shape with a median value ∼100 nA. After the first bake step, the distribution broadens, as a result of cell transitions to either lower or higher I_{read}. This is because cells first undergo the drift process, leading to a resistance increase [11], then crystallization and the consequent decrease of resistance takes place at longer times. Drift is ascribed to a structural relaxation consisting of an annihilation of defects [12], such as wrong or dangling bonds in the disordered amorphous structure. These phenomena result in an energy gap broadening over time [13] and, as a consequence, in an increase of the activation energy for conduction E_A causing the decrease of I_{read} over time. After the drift regime, crystallization first appears as a high-I_{read} tail in the current distribution. The amount of cells in the tail increases for increasing time, while the maximum I_{read} in the tail saturates to the set state.

Fig. 2 shows the time evolution of I_{read} at $T = 140$ °C for a fixed σ value, within the distributions of Fig. 1 with σ spanning the range from −3 to 3. By defining a critical current value, corresponding to the onset of crystallization ($I_x = 500$ nA), it is possible to determine the crystallization time t_x as the time in which I_{read} crosses I_x. Positive σ corresponds to fast cells, with short t_x, while negative σ are related to slow cells (long t_x). The cell-to-cell variability of crystallization time is better highlighted in the inset of Fig. 2, showing the cumulative distribution of t_x in the array at $T = 140$ °C. The t_x distribution shows a lognormal behavior, which can be explained by chemical and structural inhomogeneities in the active volume at the nanoscale [14].

Fig. 3 shows the crystallization times t_x as a function of $1/k_BT$, where k_B is the Boltzmann constant. The straight line indicates that crystallization follows an Arrhenius dependence of t_x on temperature T, with E_x being the activation energy for the crystallization process. All data show an Arrhenius behavior, with a slope E_x increasing with σ. This suggests that the t_x spread shown in the inset of Fig. 2 may be due to the cell-to-cell distribution of E_x.

IV. Cycle-to-Cycle Variability

In addition to the cell-to-cell statistical spread of crystallization behavior, individual cells generally display statistical variability from cycle-to-cycle for a given annealing condition, i.e., temperature and time. Fig. 4(a) shows the I_{read} distributions before and after annealing (3 h, 150 °C) for two consecutive set/reset/bake cycles. The postbake distribution is highly repeatable, i.e., it maintains the same shape in both cycles. However, within the distribution, there are three distinct behaviors identified by the characteristic cells I (slow crystallization), III (fast crystallization), and II (variable). Both cells I and III maintain their respective slow and fast behavior in both cycles, while cell II shows a variable behavior in each cycle. In fact, cell II has a different position within the two final distributions: during the first cycle, cell II behave similarly to cell III, thus showing a fast crystallization, while during the second cycle, cell III is close to cell I, thus showing a slower crystallization. This phenomenon reveals cycle-to-cycle variations of crystallization properties. Fig. 4(b) shows the correlation between I_{read} measured at cycle 1 and cycle 2 for all cells in the distribution of Fig. 4(a), highlighting the position of cells I, III, and II in the scatter plot. Here, the color represents the number of cells, i.e., the height of the 3-D histogram. Most of the cells (red region) are concentrated around the bisector, where the cells consistently show the same value after repeated bakes, as in the case of cells I and III. A significant fraction of cells, including cell II, is found

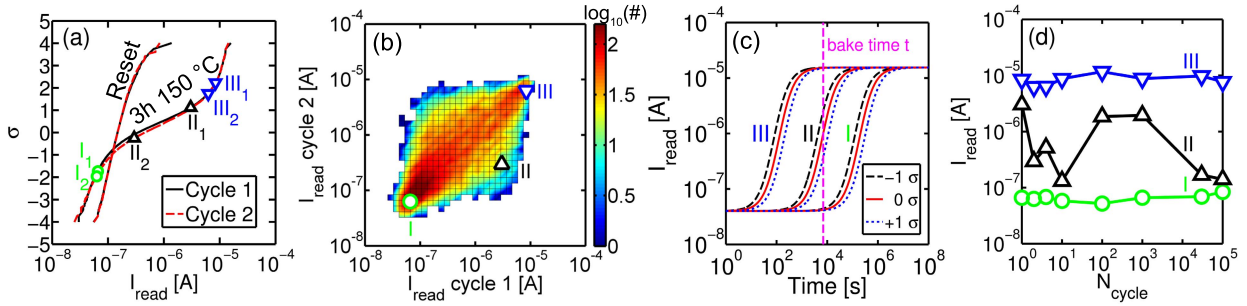

Fig. 4. (a) Reset and postbake distributions highlighting three characteristic cells: I (slow), II (variable), and III (fast). The experiment, repeated for two subsequent cycles (subscript 1 and 2), shows that cell II changes its position within the distribution, evidencing cycle-to-cycle variability. Either cell I or cell III, however, keeps their slow/fast behaviors. (b) Correlation between postbake distributions of (a) which shows the existence of cells outside of the correlation region (such as cell II). (c) All the three cells (I, II, and III) show cycle-to-cycle variability of t_x. However, this results into an I_{read} variability only when $t_x \approx t$. (d) Postbake currents show that cells I, II, and III preserve their typical slow/variable/fast behaviors for program (set/reset) cycles from 1 to 10^5.

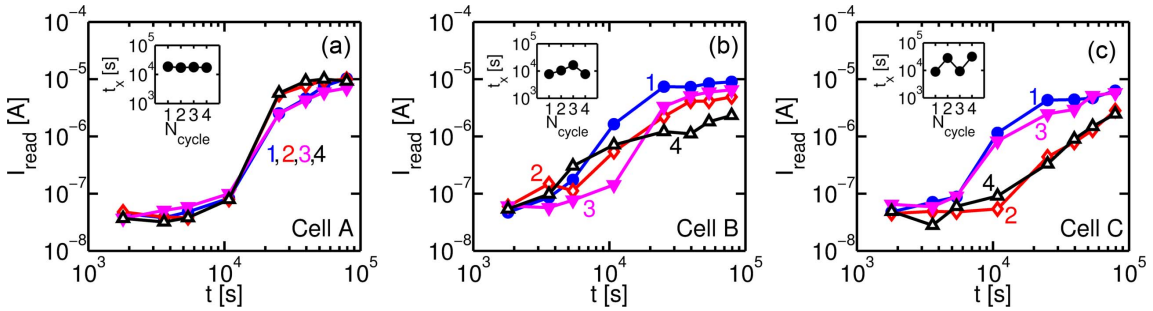

Fig. 5. Cycle-to-cycle variations in the retention curves. (a) Deterministic case: retention curves are very similar from cycle-to-cycle. (b) Analog case with random variations. (c) Digital case: retention curves digitally fluctuate between two distinct states. These variations are ascribed to reset-induced random changes in the amorphous-crystal boundary. Inset: t_x for every cycle.

outside of the correlation region because of cycle-to-cycle retention variability. These cells may show good data retention during the first cycle, while they may display fast data loss in the second one, or vice versa. Fig. 4(c) shows that all the three cells (I, II, and III) have their own cycle-to-cycle variability of t_x. However, this results into an I_{read} variability only when t_x is close to the bake time t (see cell II).

The analysis of cycle-to-cycle variability was then extended to consider a higher number N_{cycle} of set–reset cycles. Fig. 4(d) reports the postbake I_{read} as a function of N_{cycle} for cells I, III, and II. Both cells I and III maintain their slow/fast characteristics, repeatedly showing data retention/loss after every bake cycle. Cell II instead shows a fluctuating retention behavior from cycle-to-cycle.

To better understand cycle-to-cycle retention variability, Fig. 5 reports four repeated retention characteristics for three typical cells with different cycle-to-cycle variability. All characteristics generally show some level of variability in terms of crystallization time t_x and/or set-state resistance. Fig. 5(a) shows the deterministic case, i.e., the cell keeps almost the same retention curve from cycle to cycle, and therefore t_x (see inset) remains approximately constant. Fig. 5(b) shows retention characteristics where the crystallization time randomly changes from cycle-to-cycle. Finally, Fig. 5(c) shows instead a bistable transition from one characteristic to the other over the four retention experiments. We will refer to the characteristics in Fig. 5(b) and (c) as analog and digital variabilities, respectively.

Cycle-to-cycle retention variability is ascribed to the stochastic nature of the reset operation as obtained by melt-quenching. In fact, the final distribution of element/defect concentration and mechanical stresses in the amorphous network might change after each programming pulse, and thus explaining the analog variability of retention characteristics. Digital-like fluctuations can also be ascribed to the reset operation statistics. Normally, crystallization uniformly proceeds from the rim toward the center of the dome through a growth process. On the contrary, if a given grain boundary at the amorphous/crystalline interface [15] protrudes into the dome, this results in a shorter path for the crystallization growth process, hence, in a shorter t_x.

V. Monte Carlo Model for Variability

To model both the cell-to-cell and the cycle-to-cycle variability, we first described the time evolution of I_{read} according to Fig. 6(a). Here, I_{read} first decreases due to drift and then increases approaching time t_x because of crystallization. Drift was described with the classical power-law dependence [16]

$$I_{\text{reset}}(t) = I_{\text{reset}}(t_0)\left(\frac{t}{t_0}\right)^{-\nu} \tag{1}$$

where ν gives the slope of the power law and has a typical value $\nu_{\text{cycle}} = 0.1$ for full-reset states, i.e., programmed at the maximum resistance level. Crystallization was described with

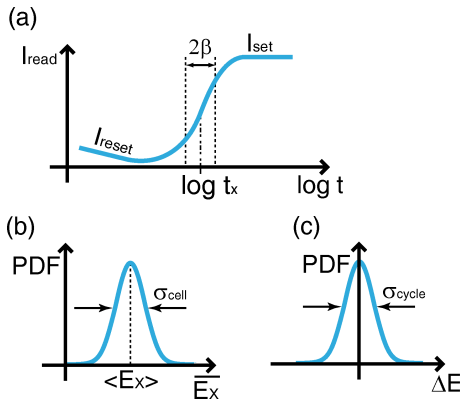

Fig. 6. MC model. (a) Initial current decrease is described through the classical drift formula reported in (1) with $\nu_{\text{cycle}} = 0.1$. Crystallization at time t_x is obtained through the empirical formulation of (2) where β, equal to 0.72, gives the slope of the transition. t_x has the Arrhenius dependence of (3) with an activation energy E_x. (b) Cell-to-cell retention variability is attributed to a Gaussian spread of E_x with standard deviation σ_{cell}. (c) Cycle-to-cycle variations are ascribed to a normal spread in E_x around zero with standard deviation σ_{cycle}. The overall E_x variability is given by the sum of the two contributions (b) and (c).

an empirical relation, given in [14]

$$I_{\text{read}} = I_{\text{reset}} + \frac{(I_{\text{set}} - I_{\text{reset}})}{2}\left[1 + \tanh\left(\frac{\log\frac{t}{t_x}}{\beta}\right)\right] \quad (2)$$

where the parameter $\beta = 0.72$ gives the slope of I_{read} transition. Based on Fig. 3, the crystallization time t_x is defined by the Arrhenius formula

$$t_x = t_0 e^{\frac{E_x}{k_B T}} = t_{00} e^{\frac{E_x}{k_B T}} e^{-\frac{E_x}{k_B T_{\text{MN}}}} \quad (3)$$

where t_{00} is a constant and E_x is the activation energy. T_{MN}, assumed equal to 680 K, is the Meyer–Neldel temperature, namely, the temperature corresponding to the crossing point of all extrapolated Arrhenius plots at variable E_x [17].

To account for the log-normal distribution of t_x in the inset of Fig. 2, we assumed a Gaussian spread of E_x, which then becomes the key parameter controlling the crystallization variability. The overall spread of E_x is given by two contributions according to

$$E_x = \overline{E_x} + \Delta E_x \quad (4)$$

where $\overline{E_x}$ is the cell-to-cell term with median value 2.85 eV and standard deviation $\sigma_{\text{cell}} = 100$ meV, as shown in Fig. 6(b). ΔE_x is the cycle-to-cycle term with average equal to zero and standard deviation σ_{cycle} of 44 meV, as shown in Fig. 6(c).

Within this interpretation, slow cells (long t_x) in the inset of Fig. 2 have a high $\overline{E_x}$, while fast cells (short t_x) are attributed to low $\overline{E_x}$. The physical origin for the cell-to-cell spread in $\overline{E_x}$ is ascribed to: 1) the spread in the local spatial arrangements of GST elements within the active volume and 2) the spread of the amorphous network configurations at the nanoscale. Given these two spread contributions, conduction in the amorphous active dome might be localized at percolation channels, due to the energy landscape of Poole–Frenkel barriers [18]. Percolation conduction might cause localized Joule heating and the consequent formation of a crystalline filament between the electrodes. The cycle-to-cycle

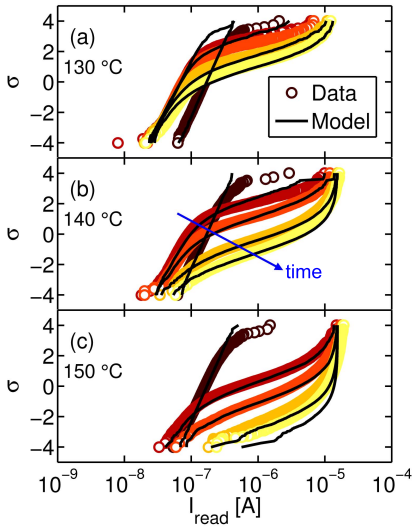

Fig. 7. Bake time dependence of I_{read} distributions at temperatures (a) 130 °C, (b) 140 °C, and (c) 150 °C. Experimental data (circles) show that increasing the bake temperatures provides a faster evolution from the initial amorphous (reset) state toward the crystalline (set) state. MC calculation results (lines) show a very good reproduction of both the current decrease due to drift and of crystallization tails.

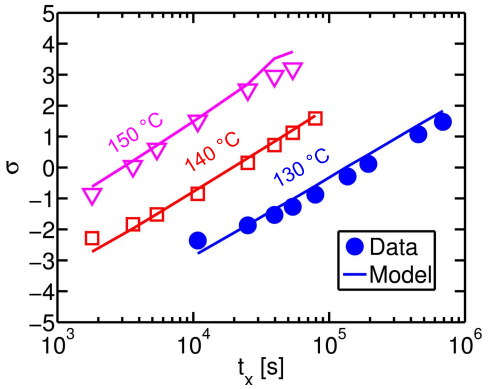

Fig. 8. t_x distributions obtained from Fig. 7 for $I_x = 500$ nA. The log-normal shape of data (symbols) is well captured by the Gaussian spread of the activation energy in the MC model (lines).

contribution ΔE_x (which does not show any significant correlation with the average E_x) may instead be attributed to the statistics of reset operation, inducing changes in the composition/defect concentration profile as explained in Section IV.

VI. Simulation Results

Our MC model allows to calculate the evolution of readout current distributions for any given time/temperature. Fig. 7 shows the distributions of measured and calculated I_{read} at 130 °C, 140 °C, and 150 °C. For increasing bake temperature, crystallization starts at increasingly shorter times t_x due to the temperature-activated phase transition kinetics [7]. The spread of E_x accounts for the shape of distributions, including both the fast crystallizing tails and the slow cells in the drift region.

From distributions in Fig. 7, it is possible to obtain t_x distributions at $I_x = 500$ nA. These are shown in Fig. 8 for increasing annealing temperature

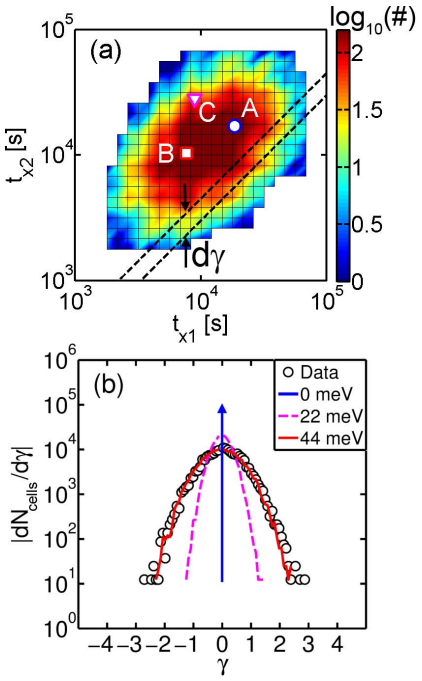

Fig. 9. (a) t_x correlation between two consecutive experiments at 150 °C in a color scale that indicates the cell density. The positions of cells A, B, and C of Fig. 5 are indicated. (b) Profile taken along the direction normal to the bisector, showing the highest cell density around the bisector line ($\gamma_{\text{cycle}} = 0$). The lines refer to MC calculations: the ideal correlation is obtained for $\sigma_{\text{cycle}} = 0$ meV while the best agreement with the experimental data is obtained for $\sigma_{\text{cycle}} = 44$ meV.

$T_{\text{cycle}} = 130$ °C, 140 °C, and 150 °C. Data and calculations were obtained from the time evolution of I_{read} in Fig. 7 at any given percentile. The median t_x decreases with temperature according to the Arrhenius formula of (3) (see also Fig. 3). Cell-to-cell t_x distributions show a normal spread on a logarithmic scale, i.e., an intrinsic t_x spread without tails. The log-normal distribution of t_x is a consequence of the normal spread in E_x.

To address the cycle-to-cycle variability or retention, Fig. 9(a) shows the correlation of t_x between two consecutive cycles, namely, t_{x1} at cycle 1 and t_{x2} at cycle 2. At the end of the first retention experiment, all the cells were reprogrammed so that the retention experiments in the first and second cycle started from the same initial distribution of the PCM array. Although most of the data show a reasonable correlation, it is possible that, due to cycle-to-cycle variability, cells show different crystallization times t_{x1} and t_{x2}. To quantify the correlation between t_{x1} and t_{x2}, we computed the cell density profile along the direction normal to the bisector. We then calculated the number N_{cells} of cells enclosed between the bisector and the line given by

$$\log(t_{x2}) = \gamma + \log(t_{x1}) \tag{5}$$

where γ is a variable. Fig. 9(b) shows the resulting $dN_{\text{cells}}/d\gamma$, which is equivalent to evaluating the cells within the infinitesimal slice between the two lines in Fig. 9(a) and dividing it by $d\gamma$ equal to 0.08. The figure shows a Gaussian distribution of N_{cells} over γ, which is representative of the cycle-to-cycle variability of crystallization time. MC simulations are also

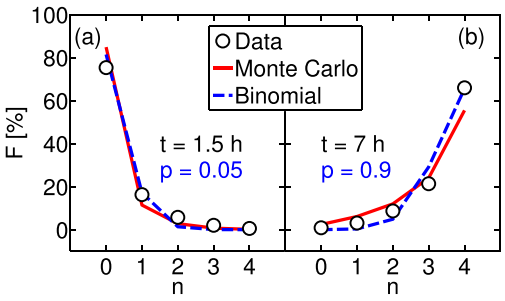

Fig. 10. Percentage of cells which shows n events of crystallization over four retention experiments. (a) About 75% of the cells never reach crystallization because of the short bake time. Only fast cells show crystallization with decreasing percentage for higher n. (b) Given the longer bake time, ~70% of the cells reach crystallization at every cycle, while only slow cells show 0, 1, 2, 3 crystallization events. Both MC and binomial results are in good agreement with the experimental data, validating the modeling approach.

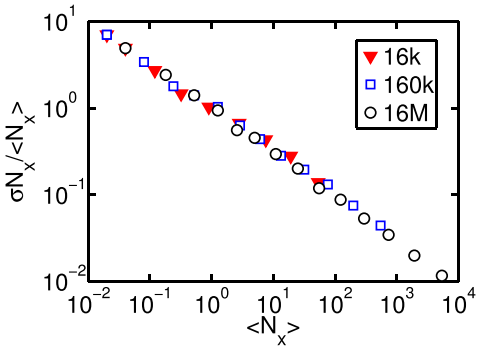

Fig. 11. Normalized standard deviation as a function of the mean number of crystallization events shows the binomial relation given by (9). The different values of $\langle N_x \rangle$ were obtained by changing I_x from 100 nA to 10 μA.

shown in Fig. 9(b), including results for $\sigma_{\text{cycle}} = 0$ meV, namely, the ideal correlation case, with delta-like distribution of $dN_{\text{cells}}/d\gamma$, and nonzero σ_{cycle}. The best agreement with the experimental results is obtained for $\sigma_{\text{cycle}} = 44$ meV, which is about one half of the cell-to-cell spread in the array.

An analytical relationship between σ_{cycle} and the spread in Fig. 9(b) σ_γ can be derived by rewriting γ using (3) and (5)

$$\gamma = \frac{E_{x2} - E_{x1}}{k_B}\left(\frac{1}{T} - \frac{1}{T_{\text{MN}}}\right). \tag{6}$$

Then, the standard deviation σ_γ of $dN_{\text{cells}}/d\gamma$ is

$$\sigma_\gamma = \frac{\sqrt{2}}{k_B}\left(\frac{1}{T} - \frac{1}{T_{\text{MN}}}\right)\sigma_{\text{cycle}}. \tag{7}$$

Using σ_{cycle} equal to 44 meV in (7), the calculated σ_γ is 0.644, very close to the experimental value 0.654 extracted from Fig. 9(b).

VII. Modeling Statistical Data Loss

The MC model can be employed as a valuable tool for the prediction of cell-to-cell data loss statistics in PCM arrays, given its capability of calculating the I_{read} distributions in Fig. 7.

Our model is also capable of predicting the cycle-to-cycle variability of data loss at any given temperature and time. Fig. 10 shows the percentage of cells that are found

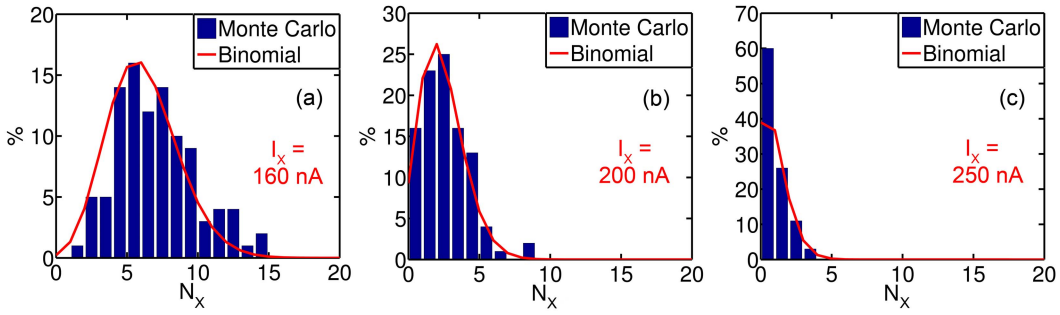

Fig. 12. N_x distributions obtained from MC calculations over a population of 16k cells. The calculations were repeated over 100 cycles for a current I_x equal to (a) 160 nA, (b) 200 nA, and (c) 250 nA. MC results are well reproduced by the analytic binomial theory with a crystallization probability p equal to (a) 3.75×10^{-4}, (b) 1.45×10^{-4}, and (c) 5.75×10^{-5}.

crystallized for a number n of times ($n = 0, 1, \ldots, 4$) within $N_{\text{trials}} = 4$ retention experiments, where cells are programmed in the reset state each time before bake. Fig. 10(a) reports the case of a short bake time ($t = 1.5$ h) for which ~75% of cells never reach crystallization during the four retention experiments ($n = 0$), while a smaller percentage of (fast) cells crystallizes $n > 0$ times. Note that F decreases at increasing n, since only a small fraction of cells with relatively short t_x show repeatable crystallization in the tail of the distribution of I_{read}. By increasing the bake time t to 7 h, most of the cells (~70%) crystallizes after every cycle ($n = 4$), while the crystallization probability decreases for decreasing n, since it is increasingly less probable that a cell crystallizes only a small number of times. The experimental results are very well reproduced by the MC model, with the same $\sigma_{\text{cycle}} = 44$ meV used in previous calculations.

Data in Fig. 10 can also be reproduced by an analytical model for the binomial probability P_n for data loss in a number of times n, given by

$$P_n = \binom{N_{\text{trials}}}{n} p^n (1-p)^{N_{\text{trials}}-n} = \frac{N_{\text{trials}}!}{n!(N_{\text{trials}}-n)!} p^n (1-p)^{N_{\text{trials}}-n} \quad (8)$$

where p is the probability of data loss in an individual retention experiment. Using a probability $p = 0.05$ for Fig. 10(a) and $p = 0.9$ for Fig. 10(b), the binomial model in (8) closely accounts for the experimental data.

A. Cycle-to-Cycle Variability of Statistical Data loss

The MC model can also be used to estimate the impact of the cycle-to-cycle retention to the crystallization tails of I_{read}. We calculated I_{read} distributions after a 800 s bake at 150 °C, for cells initially programmed in the reset state. Calculations were made considering different array populations N_{cells}, namely, 16k cells, 160k cells, and 16M cells. Simulations were repeated 100 times to investigate the cycle-to-cycle variability of crystallization. The number of crystallized cells N_x was computed as the number of cells satisfying $I_{\text{read}} > I_x$ with variable I_x. Fig. 11 shows the normalized standard deviation of the number of crystallized cells $\sigma_{N_x}/\langle N_x \rangle$ plotted as a function of the mean value $\langle N_x \rangle$. The different values of N_x were obtained by changing I_x from 100 nA to 10 μA, since by decreasing the crystallization level a larger number of cells is able to reach I_x. Irrespective of N_{cells} and of I_x, all MC simulation results overlap on a single line given by

$$\frac{\sigma_{N_x}}{\langle N_x \rangle} = \frac{1}{\langle N_x \rangle^{\frac{1}{2}}} \quad (9)$$

highlighting that the statistics can be well described by a binomial process. It is then possible to derive an analytical expression, according to the binomial statistics. Fig. 12 shows the distribution of N_x over a population of 16k cells for calculations repeated 100 cycles. The values of I_x were 160, 200, and 250 nA. For increasing I_x, the mean N_x decreases and the relative spread increases, according to the statistical Poisson distribution. Analytical results from the binomial theory are also shown, revealing its capability to reproduce MC calculations. The best fit was obtained by assuming that the crystallization probability p decreases with I_x, namely, $p = 3.75 \times 10^{-4}$, $p = 1.45 \times 10^{-4}$, and $p = 5.75 \times 10^{-5}$. This analysis allows to predict the variability of tail cells in PCM arrays over several annealing experiments.

VIII. Conclusion

Retention statistics has been characterized at both cell-to-cell and cycle-to-cycle levels in PCM arrays. Retention variability effects have been modeled through both a MC and an analytical approach. We interpreted the intrinsic ($-4/4\ \sigma$) variability as being due to a pure Gaussian spread in the activation energy for crystallization, because of cell-to-cell and cycle-to-cycle variations in composition/structure of the active amorphous volume. The model allows to predict the crystallization statistics at variable temperature and time.

References

[1] G. W. Burr, B. N. Kurdi, J. C. Scott, C. H. Lam, K. Gopalakrishnan, and R. S. Shenoy, "Overview of candidate device technologies for storage-class memory," *IBM J. Res. Develop.*, vol. 52, nos. 4–5, pp. 449–464, Jul. 2008.

[2] D. Loke *et al.*, "Breaking the speed limits of phase-change memory," *Science*, vol. 336, no. 6088, pp. 1566–1569, 2012.

[3] G. Bruns *et al.*, "Nanosecond switching in GeTe phase change memory cells," *Appl. Phys. Lett.*, vol. 95, no. 4, p. 043108, 2009.

[4] F. Xiong, A. D. Liao, D. Estrada, and E. Pop, "Low-power switching of phase-change materials with carbon nanotube electrodes," *Science*, vol. 332, no. 6029, pp. 568–570, 2011.

[5] N. Ciocchini, M. Cassinerio, D. Fugazza, and D. Ielmini, "Evidence for non-arrhenius kinetics of crystallization in phase change memory devices," *IEEE Trans. Electron Devices*, vol. 60, no. 11, pp. 3767–3774, Nov. 2013.

[6] R. Jeyasingh *et al.*, "Ultrafast characterization of phase-change material crystallization properties in the melt-quenched amorphous phase," *Nano Lett.*, vol. 14, no. 6, pp. 3419–3426, 2014.

[7] U. Russo, D. Ielmini, and A. L. Lacaita, "Analytical modeling of chalcogenide crystallization for PCM data-retention extrapolation," *IEEE Trans. Electron Devices*, vol. 54, no. 10, pp. 2769–2777, Oct. 2007.

[8] A. Redaelli, D. Ielmini, A. L. Lacaita, F. Pellizzer, A. Pirovano, and R. Bez, "Impact of crystallization statistics on data retention for phase change memories," in *IEDM Tech. Dig.*, Dec. 2005, pp. 742–745.

[9] M. Rizzi *et al.*, "Intrinsic retention statistics in phase change memory (PCM) arrays," in *IEDM Tech. Dig.*, Dec. 2013, pp. 21.7.1–21.7.3.

[10] M. Rizzi *et al.*, "Reset-induced variability of retention characteristics in phase change memory (PCM)," in *Proc. IEEE IRPS*, Jun. 2014, pp. 5E.4.1–5E.4.6.

[11] A. Pirovano, A. L. Lacaita, F. Pellizzer, S. A. Kostylev, A. Benvenuti, and R. Bez, "Low-field amorphous state resistance and threshold voltage drift in chalcogenide materials," *IEEE Trans. Electron Devices*, vol. 51, no. 5, pp. 714–719, May 2004.

[12] D. Ielmini, D. Sharma, S. Lavizzari, and A. L. Lacaita, "Reliability impact of chalcogenide-structure relaxation in phase-change memory (PCM) cells—Part I: Experimental study," *IEEE Trans. Electron Devices*, vol. 56, no. 5, pp. 1070–1077, May 2009.

[13] P. Fantini, S. Brazzelli, E. Cazzini, and A. Mani, "Band gap widening with time induced by structural relaxation in amorphous $Ge_2Sb_2Te_5$ films," *Appl. Phys. Lett.*, vol. 100, no. 1, p. 013505, 2012.

[14] D. Mantegazza, D. Ielmini, E. Varesi, A. Pirovano, and A. L. Lacaita, "Statistical analysis and modeling of programming and retention in PCM arrays," in *IEDM Tech. Dig.*, Dec. 2007, pp. 311–314.

[15] Y. H. Shih *et al.*, "Mechanisms of retention loss in $Ge_2Sb_2Te_5$-based phase-change memory," in *IEDM Tech. Dig.*, Dec. 2008, pp. 1–4.

[16] D. Ielmini, S. Lavizzari, D. Sharma, and A. L. Lacaita, "Physical interpretation, modeling and impact on phase change memory (PCM) reliability of resistance drift due to chalcogenide structural relaxation," in *IEDM Tech. Dig.*, Dec. 2007, pp. 939–942.

[17] A. Yelon, B. Movaghar, and H. Branz, "Origin and consequences of the compensation (Meyer–Neldel) law," *Phys. Rev. B*, vol. 46, no. 19, pp. 12244–12250, 1992.

[18] M. Rizzi, M. Ferro, P. Fantini, and D. Ielmini, "Energy landscape model of conduction and phase transition in phase change memories," *IEEE Trans. Electron Devices*, vol. 60, no. 11, pp. 3618–3624, Nov. 2013.